Communications in Analysis and Mechanics

https://www.aimspress.com/journal/cam

Communications in Analysis and Mechanics, 18(1): 228–244.
DOI: 10.3934/cam.2026009
Received: 04 August 2025
Revised: 12 October 2025
Accepted: 04 January 2026
Published: 16 March 2026

Research article

Topological derivative for a fast identification of short, linear perfectly conducting cracks with inaccurate background information

Won-Kwang Park*

Department of Information Security, Cryptography, and Mathematics, Kookmin University, Seoul, 02707, Korea

* **Correspondence:** Email: parkwk@kookmin.ac.kr.

Abstract: In this study, we consider a topological derivative-based imaging technique for the fast identification of short, linear perfectly conducting cracks completely embedded in a two-dimensional homogeneous domain with smooth boundary. Unlike conventional approaches, we assume that the background permittivity and permeability are unknown due to their dependence on frequency and temperature, and we propose a normalized imaging function to localize cracks. Despite inaccuracies in background parameters, application of the proposed imaging function enables recognition of the existence of cracks, but it is still impossible to identify accurate crack locations. Furthermore, the shift in crack localization of imaging results is significantly influenced by the applied background parameters. In order to theoretically explain this phenomenon, we show that the imaging function can be expressed in terms of the zero-order Bessel function of the first kind, the crack lengths, and the applied inaccurate background wavenumber corresponding to the applied inaccurate background permittivity and permeability. Various numerical simulation results with synthetic data polluted by random noise validate the theoretical results.

Keywords: topological derivative; inaccurate background information; Bessel function; numerical simulation results; perfectly conducting cracks
Mathematics Subject Classification: 78A46

1. Introduction

Accurate and efficient identification of unknown defects from scattering phenomena by applying microwaves is of paramount importance in various engineering and physical applications, including non-destructive testing [1–3], structural health monitoring [4–6], biomedical imaging [7–9], and radar technology [10–12]. Due to the fundamental nonlinearity and ill-posedness of the problem, various iterative (quantitative) inversion techniques have been developed to address microwave imaging chal-

lenges. Examples include Newton-type shape reconstruction for arc-like cracks [13], Gauss–Newton method for breast cancer imaging [14], Born iterative approach for brain stroke detection [15], level set method for retrieving the shape of unknown scatterers [16], Newton–Kantorovich method for arm and thorax imaging [17], and optimal control approach for shape reconstruction of extended scatterers [18]. Although these iterative-based inversion techniques have been successfully applied to various real-world microwave imaging problems, several critical issues, such as non-convergence phenomena, entrapment in local minima, and significant computational costs due to the large number of iterations, may arise if the iterative process is initiated without a good initial guess and prior information of unknown targets. Moreover, because iterative-based techniques are highly sensitive to measurement noise, this can lead to substantial errors in the reconstructed results so that appropriate regularization strategies must be adopted. Hence, for obtaining a good initial guess or prior information (location, shape, etc.) of unknown objects, various non-iterative (qualitative) inversion techniques have been investigated.

Among the many available non-iterative techniques, topological derivative-based imaging methods have drawn significant attention. Originally, this was investigated for the shape optimization problem [19], but its application for fast identification of unknown objects in inverse scattering problems has been demonstrated successfully; for example, previous studies have addressed the fast identification of small cracks using higher-order topological derivatives [20]; the detection of small defects through a fast non-iterative method [21]; fast imaging of thin, curve-like electromagnetic inhomogeneities [22]; non-iterative imaging of three-dimensional penetrable obstacles [23]; multi-frequency topological derivatives for flaw detection in welding joints [24]; one-step imaging of homogeneous two- and three-dimensional targets from Fresnel experimental datasets [25]; the identification of three-dimensional hard obstacles from acoustic waves [26]; localization of anisotropic scatterers embedded in anisotropic backgrounds [27]; and infrared thermography for detecting defects inside thin plates [28]. We also refer to [29–33] for various remarkable results about the topological derivatives.

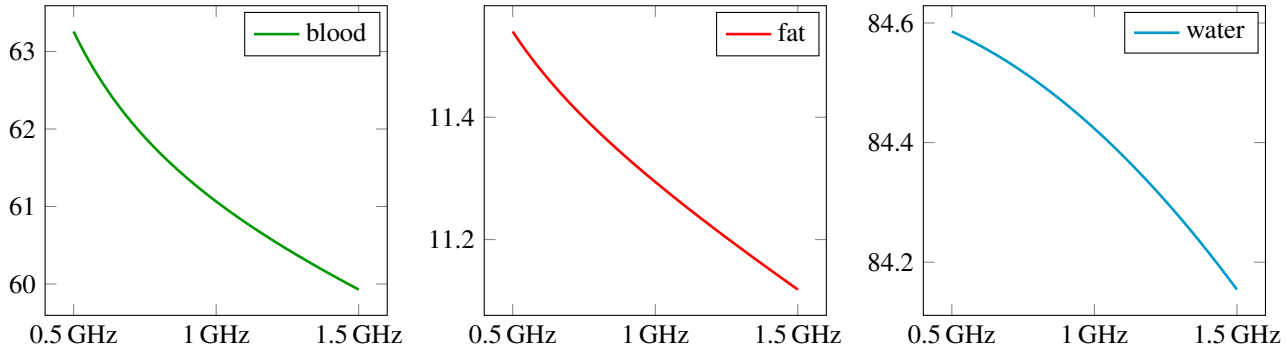

Figure 1. Permittivity values of blood, fat, and water between $f = 0.5$ GHz and $f = 1.5$ GHz.

In general, the effectiveness of topological derivative methods hinges on the accurate knowledge of background material properties—specifically, the permittivity, permeability, and conductivity of the medium. However, in real-world applications, such parameters are often inaccurately known due to their sensitivity to environmental variations such as temperature and operating frequency. Related works can be found in [34–38], and we refer to Figure 1. This leads to critical issues in practical implementations, where even slight deviations from true background values cause inaccurate imaging results. However, to the best of our knowledge, a reliable mathematical theory has not been investigated to explain this phenomenon.

To address this issue, we consider the application of a topological derivative for identifying a set of two-dimensional short, linear perfectly conducting cracks completely embedded in a homogeneous medium, even when accurate background permittivity or permeability values are unknown. To this end, we introduce a topological derivative-based imaging function based on a misfit functional with inaccurate permittivity and permeability values. In order to explain some phenomena, including the appearance of inaccurate locations of cracks, we carefully investigate the structure of the imaging function by establishing its relationship with crack length, both accurate and inaccurate wavenumbers, and the zero-order Bessel function. This is based on the fact that the boundary measurement data can be expressed by the asymptotic expansion formula in the presence of small cracks. To validate the theoretical results, numerical simulation results with boundary measurement data corrupted by random noise in the existence of single and multiple short, linear cracks are exhibited.

This paper is organized as follows: In Section 2, we introduce the basic concept of the forward problem in the presence of a set of short, linear perfectly conducting cracks and design a topological derivative-based imaging function with an inaccurate background wavenumber corresponding to the applied permittivity and permeability values. In Section 3, we explore the mathematical structure of the designed imaging function and discuss its various properties, including the appearance of inaccurate results. In Section 4, we present numerical simulation results to validate the theoretical result. In Section 5, a short conclusion including future directions is provided.

2. Topological derivative-based imaging

Let Γ_m be an open, linear perfectly conducting crack with length $2\ell_m$ and center $\mathbf{x}_m$, and Γ denotes the collection of Γ_m. Throughout this paper, all Γ_m are completely embedded in a homogeneous bounded material $\Omega \subset \mathbb{R}^2$ with smooth boundary $\partial\Omega \in C^2$, permittivity ε_b, and permeability μ_b at given angular frequency $\omega = 2\pi f$. We further assume that Ω is a subset of the anechoic chamber; thus, $\mu_\mathrm{b} = 4\pi \times 10^{-7}\,\mathrm{H/m}$, $\varepsilon_\mathrm{b} = 8.854 \times 10^{-12}\,\mathrm{F/m}$, and the background conductivity $\sigma_\mathrm{b} \approx 0$. By denoting $k = \omega\sqrt{\varepsilon_\mathrm{b}\mu_\mathrm{b}}$ and λ as the background wavenumber and given positive wavelength, respectively, we assume that

$$k|\mathbf{x}_m - \mathbf{x}_{m'}| \gg \frac{1}{4} \quad \text{and} \quad \ell_m < \frac{\lambda}{2}, \tag{2.1}$$

for $m, m' = 1, 2, \ldots, M$ and $m \neq m'$. These conditions mean that all Γ_m are sufficiently separated from each other and their lengths are short. Furthermore, we assume that Γ_m does not touch the $\partial\Omega$, i.e., there is a positive constant C such that

$$\mathrm{dist}(\Gamma_m, \partial\Omega) \geq C.$$

In the presence of Γ, let $u^{(n)}(\mathbf{x}; k)$ be the time-harmonic total field satisfying the boundary value problem

$$\begin{cases} \triangle u^{(n)}(\mathbf{x}; k) + k^2 u^{(n)}(\mathbf{x}; k) = 0 \quad \text{in} \quad \Omega\backslash\overline{\Gamma}, \\ u^{(n)}(\mathbf{x}; k) = 0 \quad \text{on} \quad \Gamma, \\ \dfrac{\partial u^{(n)}(\mathbf{x}; k)}{\partial \boldsymbol{\nu}(\mathbf{x})} = \dfrac{\partial \exp(ik\boldsymbol{\theta}_n \cdot \mathbf{x})}{\partial \boldsymbol{\nu}(\mathbf{x})} = g^{(n)}(\mathbf{x}) \in L^2(\partial\Omega) \quad \text{on} \quad \partial\Omega, \end{cases} \tag{2.2}$$

where $\boldsymbol{\nu}(\mathbf{x})$ is the outward normal to $\mathbf{x} \in \partial\Omega$ and $\boldsymbol{\theta}_n \in \mathbb{S}^1$, $n = 1, 2, \ldots, N$ denotes the propagation direction. We assume that k^2 is not an eigenvalue for the operator $-\triangle$ in $L^2(\Omega)$ to guarantee the

well-posedness and all $\boldsymbol{\theta}_n$ are uniformly distributed on $\mathbb{S}^1$ such that

$$\boldsymbol{\theta}_n = (\cos\theta_n, \sin\theta_n) = \left(\cos\frac{2(n-1)\pi}{N}, \sin\frac{2(n-1)\pi}{N}\right), \quad n = 1, 2, \ldots, N. \tag{2.3}$$

Analogously, let $w^{(n)}(\mathbf{x}; k) = \exp(ik\boldsymbol{\theta}_n \cdot \mathbf{x})$ be the background solution, which satisfies (2.2) in the absence of Γ.

Now, let us consider the following misfit functional, which depends on the solution $u^{(n)}(\mathbf{x}; k)$:

$$\mathbb{E}(\Omega) = \frac{1}{2}\sum_{n=1}^{N}\int_{\partial\Omega} |u^{(n)}(\mathbf{x}; k) - w^{(n)}(\mathbf{x}; k)|^2 \mathrm{d}\mathbf{x}. \tag{2.4}$$

In order to introduce the topological derivative-based imaging function, let us create a small linear crack Σ with length ϵ at $\mathbf{z} \in \Omega\backslash\partial\Omega$ and denote $\Omega\backslash\Sigma$ as the corresponding domain. Similar to (2.2), we denote $u_\epsilon^{(n)}(\mathbf{x}; k)$ as the time-harmonic total field that satisfies the boundary value problem

$$\begin{cases} \triangle u_\epsilon^{(n)}(\mathbf{x}; k) + k^2 u_\epsilon^{(n)}(\mathbf{x}; k) = 0 \quad \text{in} \quad \Omega\backslash\overline{\Sigma}, \\ u_\epsilon^{(n)}(\mathbf{x}; k) = 0 \quad \text{on} \quad \Sigma, \\ \dfrac{\partial u_\epsilon^{(n)}(\mathbf{x}; k)}{\partial \boldsymbol{\nu}(\mathbf{x})} = \dfrac{\partial \exp(ik\boldsymbol{\theta}_n \cdot \mathbf{x})}{\partial \boldsymbol{\nu}(\mathbf{x})} = g^{(n)}(\mathbf{x}) \in L^2(\partial\Omega) \quad \text{on} \quad \partial\Omega, \end{cases}$$

and define $\mathbb{E}(\Omega\backslash\Sigma)$ as the following misfit functional:

$$\mathbb{E}(\Omega\backslash\Sigma) = \frac{1}{2}\sum_{n=1}^{N}\int_{\partial\Omega} |u_\epsilon^{(n)}(\mathbf{x}; k) - w^{(n)}(\mathbf{x}; k)|^2 \mathrm{d}\mathbf{x}.$$

Since the creation of Σ changes the topology of the entire domain Ω, it is natural to consider the corresponding topological derivative $d_T\mathbb{E}(\mathbf{z})$ of $\mathbb{E}(\Omega)$ with respect to point $\mathbf{z}$ such that

$$d_T\mathbb{E}(\mathbf{z}) = \lim_{\epsilon\to 0+} \frac{\mathbb{E}(\Omega\backslash\Sigma) - \mathbb{E}(\Omega)}{\varphi(\epsilon)}, \tag{2.5}$$

where $\varphi(\epsilon) \longrightarrow 0$ as $\epsilon \longrightarrow 0+$. From (2.5), we obtain the asymptotic expansion

$$\mathbb{E}(\Omega\backslash\Sigma) = \mathbb{E}(\Omega) + \varphi(\epsilon) d_T\mathbb{E}(\mathbf{z}) + o(\varphi(\epsilon)). \tag{2.6}$$

Based on [39], we can explore forms of $\varphi(\epsilon)$ and $d_T\mathbb{E}(\mathbf{z})$ as follows.

Lemma 2.1. *Let $\mathbb{E}(\Omega)$ be defined as* (2.4)*. Then, $\varphi(\epsilon)$ and $d_T\mathbb{E}(\mathbf{z})$ are written as*

$$\varphi(\epsilon) = \frac{2\pi}{\ln(\epsilon/2)} \quad \textit{and} \quad d_T\mathbb{E}(\mathbf{z}) = \mathrm{Re}\sum_{n=1}^{N} v^{(n)}(\mathbf{z}; k)\overline{w^{(n)}(\mathbf{z}; k)}, \tag{2.7}$$

respectively. Here, $v^{(n)}(\mathbf{x}; k)$ satisfies the adjoint problem

$$\begin{cases} \Delta v^{(n)}(\mathbf{x}; k) + k^2 v^{(n)}(\mathbf{x}; k) = 0 \quad \textit{in} \quad \Omega, \\ \dfrac{\partial v^{(n)}(\mathbf{x}; k)}{\partial \boldsymbol{\nu}(\mathbf{x})} = u^{(n)}(\mathbf{x}; k) - w^{(n)}(\mathbf{x}; k) \quad \textit{on} \quad \partial\Omega. \end{cases} \tag{2.8}$$

Remark 2.1. The expression of φ depends on the type of generated object. For example, if a small circular inclusion with radius α and conductivity σ is generated, φ is given by (see [40] for derivation)

$$\varphi(\alpha) = -2\pi\alpha^2\left(\frac{\sigma-\sigma_0}{\sigma+\sigma_0}\right).$$

Details on the φ with respect to the generated inclusion can be found in the recent studies [24,25,39,41–43].

Based on prior studies [20, 22, 23, 25, 39, 44], the existence and location of Γ_m can be identified through the map of $d_T\mathbb{E}(\mathbf{z})$. However, for a successful application of $d_T\mathbb{E}(\mathbf{z})$, exact values of ε_b and μ_b must be known. But, since the values of ε_b and μ_b are dependent on the applied frequency and ambient temperature, it will be inappropriate to apply (2.7) without prior information of exact ε_b and μ_b.

Since the accurate value of k is unknown, let us apply alternative background wavenumber $k_\mathrm{a} = \omega\sqrt{\varepsilon_\mathrm{a}\mu_\mathrm{a}}$ with inaccurate permittivity ε_a and permeability μ_a, and introduce the following normalized topological derivative-based imaging function:

$$\mathfrak{F}(\mathbf{z};k_\mathrm{a}) = \frac{|d_T\mathbb{E}(\mathbf{z};k_\mathrm{a})|}{\max\limits_{\mathbf{z}\in\Omega}|d_T\mathbb{E}(\mathbf{z};k_\mathrm{a})|} \quad \text{where} \quad d_T\mathbb{E}(\mathbf{z};k_\mathrm{a}) = \mathrm{Re}\sum_{n=1}^{N} v^{(n)}(\mathbf{z};k_\mathrm{a})\overline{w^{(n)}(\mathbf{z};k_\mathrm{a})}, \tag{2.9}$$

where $w^{(n)}(\mathbf{x};k_\mathrm{a}) = \exp(ik_\mathrm{a}\boldsymbol{\theta}_n\cdot\mathbf{x})$ and $v^{(n)}(\mathbf{x};k_\mathrm{a})$ satisfies the adjoint problem

$$\begin{cases} \Delta v^{(n)}(\mathbf{x};k_\mathrm{a}) + k_\mathrm{a}^2 v^{(n)}(\mathbf{x};k_\mathrm{a}) = 0 \quad \text{in} \quad \Omega, \\ \dfrac{\partial v^{(n)}(\mathbf{x};k_\mathrm{a})}{\partial\boldsymbol{\nu}(\mathbf{x})} = u^{(n)}(\mathbf{x};k) - w^{(n)}(\mathbf{x};k) \quad \text{on} \quad \partial\Omega. \end{cases} \tag{2.10}$$

Same as in (2.2), we also assume that k_a^2 is not an eigenvalue for the operator $-\triangle$ in $L^2(\Omega)$. Fortunately, based on simulation results in Section 4, the existence of Γ_m can be recognized through the map of $\mathfrak{F}(\mathbf{z};k_\mathrm{a})$ even if $k_\mathrm{a}\neq k$, but the identified location $\mathbf{x}_m\in\Gamma_m$ is shifted in a specific direction. However, to the best of our knowledge, the mathematical background to support this has not been established yet.

3. Structure of the imaging function

In this section, we explore the mathematical structure of the topological derivative-based imaging function $\mathfrak{F}(\mathbf{z};k_\mathrm{a})$ and discuss its various properties. To this end, we recall the asymptotic expansion formula derived in [45]. We also refer to [46–52] for several asymptotic expansions related to boundary value problems in domains with small holes and arc-like inclusions.

Lemma 3.1 (Asymptotic expansion formula)**.** *Let $u^{(n)}(\mathbf{x};k)$ satisfy* (2.2) *and $w^{(n)}(\mathbf{x};k)$ be the background solution of* (2.2)*. Then, if the condition* (2.1) *is valid, the following asymptotic expansion formula holds uniformly on $\mathbf{x}\in\partial\Omega$:*

$$u^{(n)}(\mathbf{x};k) - w^{(n)}(\mathbf{x};k) = \sum_{m=1}^{M}\frac{2\pi}{\ln(\ell_m/2)}w^{(n)}(\mathbf{x}_m;k)\mathcal{N}(\mathbf{x},\mathbf{x}_m;k) + O\left(\frac{1}{|\ln\ell_m|^2}\right), \tag{3.1}$$

where $\mathcal{N}$ denotes the Neumann function, which satisfies

$$\begin{cases} \Delta\mathcal{N}(\mathbf{x},\mathbf{z};k) + k^2\mathcal{N}(\mathbf{x},\mathbf{z};k) = -\delta(\mathbf{x},\mathbf{z}) \quad \textit{in} \quad \Omega, \\ \dfrac{\partial\mathcal{N}(\mathbf{x},\mathbf{z};k)}{\partial\boldsymbol{\nu}(\mathbf{x})} = 0 \quad \textit{on} \quad \partial\Omega. \end{cases}$$

Here, δ is the Dirac delta function.

Now, we derive the main result. For the sake derivation, we remove the term $O(|\ln \ell_m|^{-2})$ from (3.1) in the derivation of the following result.

Theorem 3.1. *For sufficiently large N, $\mathfrak{F}(\mathbf{z}; k_a)$ can be represented as follows:*

$$\mathfrak{F}(\mathbf{z}; k_a) \approx \frac{|\Phi(\mathbf{z})|}{\max\limits_{\mathbf{z}\in\Omega} |\Phi(\mathbf{z})|}, \quad \Phi(\mathbf{z}) = \sum_{m=1}^{M} \frac{J_0(|k\mathbf{x}_m - k_a\mathbf{z}|)}{\ln(\ell_m/2)}, \tag{3.2}$$

where J_0 is the zero-order Bessel function of the first kind.

Proof. Since $v^{(n)}(\mathbf{x}; k_a)$ satisfies (2.10), for $\mathbf{z} \in \Omega\backslash\partial\Omega$, we have

$$v^{(n)}(\mathbf{z}; k_a) = \int_{\partial\Omega} \frac{v^{(n)}(\mathbf{x}; k_a)}{\partial \boldsymbol{\nu}(\mathbf{x})} \mathcal{N}(\mathbf{x}, \mathbf{z}; k_a) d\mathbf{x} = \int_{\partial\Omega} \left(u^{(n)}(\mathbf{x}; k) - w^{(n)}(\mathbf{x}; k)\right) \mathcal{N}(\mathbf{x}, \mathbf{z}; k_a) d\mathbf{x}. \tag{3.3}$$

Applying (3.1) and (3.3) to (2.9), we can obtain

$$\begin{aligned} d_T \mathbb{E}(\mathbf{z}; k_a) &= \mathrm{Re} \sum_{n=1}^{N} v^{(n)}(\mathbf{z}; k_a) \overline{w^{(n)}(\mathbf{z}; k_a)} \\ &\approx \Re\mathrm{e} \sum_{n=1}^{N} \left[\int_{\partial\Omega} \left(u^{(n)}(\mathbf{x}; k) - w^{(n)}(\mathbf{x}; k)\right) \mathcal{N}(\mathbf{x}, \mathbf{z}; k_a) d\mathbf{x} \right] \overline{w^{(n)}(\mathbf{z}; k_a)} \\ &\approx \Re\mathrm{e} \sum_{n=1}^{N} \left[\int_{\partial\Omega} \left(\sum_{m=1}^{M} \frac{2\pi}{\ln(\ell_m/2)} w^{(n)}(\mathbf{x}_m; k) \mathcal{N}(\mathbf{x}, \mathbf{x}_m; k) \right) \mathcal{N}(\mathbf{x}, \mathbf{z}; k_a) d\mathbf{x} \right] \overline{w^{(n)}(\mathbf{z}; k_a)} \\ &= \Re\mathrm{e} \sum_{m=1}^{M} \frac{2\pi}{\ln(\ell_m/2)} \left(\int_{\partial\Omega} \mathcal{N}(\mathbf{x}, \mathbf{x}_m; k) \mathcal{N}(\mathbf{x}, \mathbf{z}; k_a) d\mathbf{x} \right) \left(\sum_{n=1}^{N} w^{(n)}(\mathbf{x}_m; k) \overline{w^{(n)}(\mathbf{z}; k_a)} \right). \end{aligned} \tag{3.4}$$

Since $\boldsymbol{\theta}_n$ is defined as in (2.3), the following relationship holds for sufficiently large N, $\mathbf{x} = |\mathbf{x}|(\cos\phi, \sin\phi)$ and $\triangle\theta = 2\pi/N$ (see [53] for derivation):

$$\begin{aligned} \sum_{n=1}^{N} \exp(\boldsymbol{\theta}_n \cdot \mathbf{x}) &= \frac{N}{2\pi} \sum_{n=1}^{N} \exp\left(|\mathbf{x}| \cos(\theta_n - \phi)\right) \triangle\theta \approx \frac{N}{2\pi} \int_0^{2\pi} \exp\left(|\mathbf{x}| \cos(\theta - \phi)\right) d\theta \\ &= \frac{N}{2\pi} \int_0^{2\pi} \left(J_0(|\mathbf{x}|) + 2 \sum_{p=1}^{\infty} i^p J_p(|\mathbf{x}|) \cos\left(p(\theta - \phi)\right) \right) d\theta = N J_0(|\mathbf{x}|). \end{aligned}$$

With this, we can derive

$$\sum_{n=1}^{N} w^{(n)}(\mathbf{x}_m; k) \overline{w^{(n)}(\mathbf{z}; k_a)} = \sum_{n=1}^{N} \exp\left(\boldsymbol{\theta}_n \cdot (k\mathbf{x}_m - k_a\mathbf{z})\right) \approx N J_0(|k\mathbf{x}_m - k_a\mathbf{z}|). \tag{3.5}$$

Next, following to [47], the Neumann function $\mathcal{N}$ has a logarithmic singularity. Thus, it can be decomposed into the singular and regular functions

$$\mathcal{N}(\mathbf{x}, \mathbf{z}; k) = -\frac{1}{2\pi} \ln|\mathbf{x} - \mathbf{z}| + \mathcal{R}(\mathbf{x}, \mathbf{z}; k), \quad \mathbf{x} \neq \mathbf{z},$$

where $\mathcal{R}(\mathbf{x},\mathbf{z};k)\in C^{1,\alpha}$ in both $\mathbf{x}$ and $\mathbf{y}$ for some α with $0<\alpha<1$. Since $\mathbf{x}\in\partial\Omega$ and $\mathbf{x}_m\in\Gamma_m$, there is no blow up of $\mathcal{N}(\mathbf{x},\mathbf{x}_m;k)$ so that

$$|\mathcal{N}(\mathbf{x},\mathbf{x}_m;k)|\le\frac{1}{2\pi}\ln|\mathbf{x}-\mathbf{x}_m|+|\mathcal{R}(\mathbf{x},\mathbf{x}_m;k)|<\frac{1}{2\pi}\ln\mathrm{diam}(\Omega)+\max_{\mathbf{x}\in\partial\Omega}|\mathcal{R}(\mathbf{x},\mathbf{x}_m;k)|,$$

where $\mathrm{diam}(\Omega)$ denotes the diameter of Ω. Hence, applying Hölder's inequality yields

$$\left|\int_{\partial\Omega}\mathcal{N}(\mathbf{x},\mathbf{x}_m;k)\mathcal{N}(\mathbf{x},\mathbf{z};k_{\mathrm{a}})\mathrm{d}\mathbf{x}\right|\le\left(\frac{1}{2\pi}\ln\mathrm{diam}(\Omega)+\max_{\mathbf{x}\in\partial\Omega}|\mathcal{R}(\mathbf{x},\mathbf{x}_m;k)|\right)\int_{\partial\Omega}|\mathcal{N}(\mathbf{x},\mathbf{z};k_{\mathrm{a}})|\mathrm{d}\mathbf{x}.$$

Now, we consider the singularity of $\mathcal{N}(\mathbf{x},\mathbf{z};k_{\mathrm{a}})$ when $\mathbf{z}\in\Omega$ is close to $\mathbf{x}\in\partial\Omega$. To this end, for sufficiently small constant $\rho>0$, generate a ball $B(\mathbf{x},\rho)$ with radius ρ and center $\mathbf{x}$ such that

$$B(\mathbf{x},\rho)\cap\Gamma=\varnothing.$$

Based on this, let us split $\partial\Omega$ into two smooth curves, $\partial\Omega=\partial\Omega_{\mathrm{sing}}\cup\partial\Omega_{\mathrm{reg}}$ (see Figure 2 for illustration), where

$$\partial\Omega_{\mathrm{sing}}=\Omega\cap\partial B(\mathbf{x},\rho)\quad\text{and}\quad\partial\Omega_{\mathrm{reg}}=\partial\Omega\backslash\overline{\partial\Omega_{\mathrm{sing}}}.$$

Then, we can examine that

$$\begin{aligned}\int_{\partial\Omega}|\mathcal{N}(\mathbf{x},\mathbf{z};k_{\mathrm{a}})|\mathrm{d}\mathbf{x}\le&\frac{1}{2\pi}\int_{\partial\Omega}\ln|\mathbf{x}-\mathbf{z}|\mathrm{d}\mathbf{x}+\int_{\partial\Omega}|\mathcal{R}(\mathbf{z},\mathbf{y};\omega)|\mathrm{d}\mathbf{x}\\
\le&\frac{1}{2\pi}\lim_{\rho\to0+}\left(\int_{\partial\Omega_S}\ln|\mathbf{x}-\mathbf{z}|\mathrm{d}\mathbf{x}+\int_{\partial\Omega_R}\ln|\mathbf{x}-\mathbf{z}|\mathrm{d}\mathbf{x}\right)+\max_{\mathbf{x}\in\partial\Omega}|\mathcal{R}(\mathbf{x},\mathbf{z};k_{\mathrm{a}})|\,\mathrm{length}(\partial\Omega)\\
\le&\frac{1}{2\pi}\lim_{\rho\to0+}\Big(\rho\ln\rho+(\mathrm{length}(\partial\Omega)-\rho)\ln|\,\mathrm{length}(\partial\Omega)|\Big)+\max_{\mathbf{x}\in\partial\Omega}|\mathcal{R}(\mathbf{x},\mathbf{z};k_{\mathrm{a}})|\,\mathrm{length}(\partial\Omega)\\
=&\,\mathrm{length}(\partial\Omega)\Big(\frac{1}{2\pi}\ln|\,\mathrm{length}(\partial\Omega)|+\max_{\mathbf{x}\in\partial\Omega}|\mathcal{R}(\mathbf{x},\mathbf{z};k_{\mathrm{a}})|\Big).\end{aligned}$$

Here, $\mathrm{length}(\partial\Omega)$ denotes the length of $\partial\Omega$. Therefore,

$$\begin{aligned}\left|\int_{\partial\Omega}\mathcal{N}(\mathbf{x},\mathbf{x}_m;k)\mathcal{N}(\mathbf{x},\mathbf{z};k_{\mathrm{a}})\mathrm{d}\mathbf{x}\right|\le&\left(\frac{1}{2\pi}\ln\mathrm{diam}(\Omega)+\max_{\mathbf{x}\in\partial\Omega}|\mathcal{R}(\mathbf{x},\mathbf{x}_m;k)|\right)\\
&\times\mathrm{length}(\partial\Omega)\Big(\frac{1}{2\pi}\ln|\,\mathrm{length}(\partial\Omega)|+\max_{\mathbf{x}\in\partial\Omega}|\mathcal{R}(\mathbf{x},\mathbf{z};k_{\mathrm{a}})|\Big).\end{aligned}\tag{3.6}$$

This means that there is no blowup of $\int_{\partial\Omega}\mathcal{N}(\mathbf{x},\mathbf{x}_m;k)\mathcal{N}(\mathbf{x},\mathbf{z};k_{\mathrm{a}})\mathrm{d}\mathbf{x}$ for any $\mathbf{x}\in\partial\Omega$ and $\mathbf{z}\in\Omega$.

Plugging (3.5) and (3.6) into (3.4), we can examine that

$$d_T\mathbb{E}(\mathbf{z};k_{\mathrm{a}})\propto\sum_{m=1}^{M}\frac{J_0(|k\mathbf{x}_m-k_{\mathrm{a}}\mathbf{z}|)}{\ln(\ell_m/2)},$$

and correspondingly, (3.2) can be obtained. □

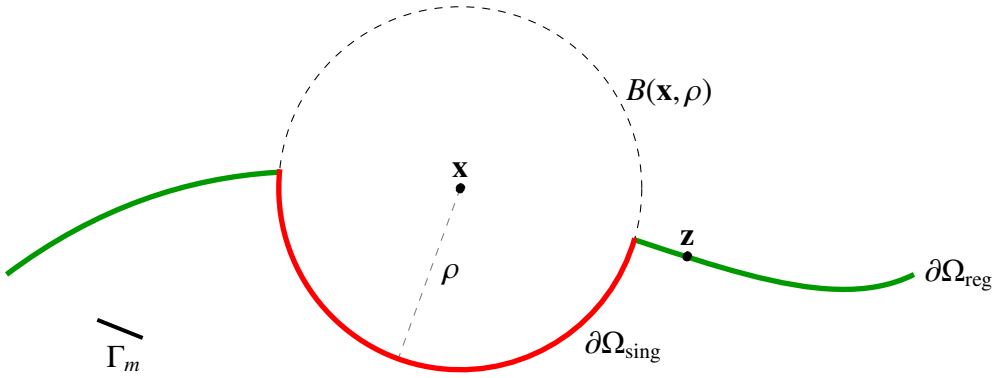

Figure 2. Illustration of $\partial\Omega_{\text{sing}}$ and $\partial\Omega_{\text{reg}}$.

Now, we discuss some properties of $\mathfrak{F}(\mathbf{z};k_{\text{a}})$ based on Theorem 3.1.

Property 3.1 (Identification of inaccurate location and shape). Since $J_0(x)$ has its maximum value 1 at $x=0$, the location $\mathbf{z}=(k/k_{\text{a}})\mathbf{x}_m$, $m=1,2,\ldots,M$ will be identified through the map of $\mathfrak{F}(\mathbf{z};k_{\text{a}})$ instead of the true location $\mathbf{x}_m\in\Gamma_m$. Hence, although the existence of cracks can be recognized, their exact location cannot be determined unless the exact values of ε_{b} and μ_{b} are known.

Property 3.2 (Observation of shifting effect when applying inaccurate permittivity). Assume that $\varepsilon_{\text{a}}\neq\varepsilon_{\text{b}}$, $\mu_{\text{a}}=\mu_{\text{b}}$, and k_{a} satisfies (2.1). Then, for $\mathbf{x}_m\in\Sigma_m$, identified location $\mathbf{z}$ becomes

$$\mathbf{z}=\left(\frac{k}{k_{\text{a}}}\right)\mathbf{x}_m=\sqrt{\frac{\varepsilon_{\text{b}}}{\varepsilon_{\text{a}}}}\mathbf{x}_m.$$

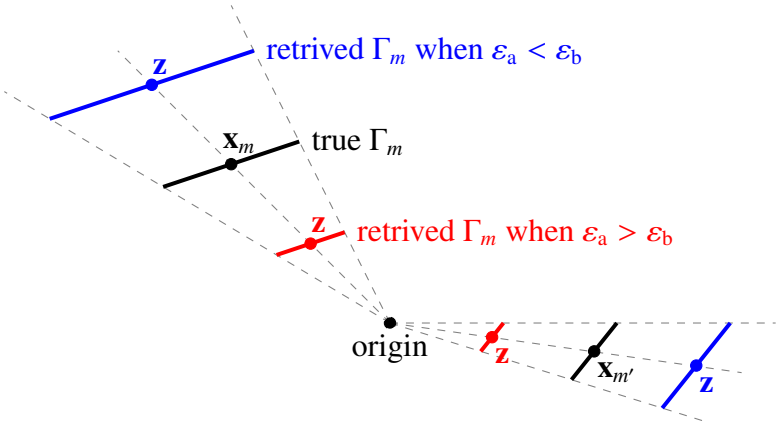

Figure 3. (Property 3.2) Illustration of simulation results. Black-colored straight lines are true cracks, and blue- and red-colored straight lines are retrieved cracks when $\varepsilon_{\text{a}}<\varepsilon_{\text{b}}$ and $\varepsilon_{\text{a}}>\varepsilon_{\text{b}}$, respectively.

Hence, the retrieved location and length of Γ_m will be close to the origin and shorter than the true Γ_m, respectively, when $\varepsilon_{\text{a}}>\varepsilon_{\text{b}}$ (refer to the red-colored straight lines in Figure 3). Otherwise, the retrieved location and length of Γ_m will be far away from the origin and longer than the true Γ_m, respectively, when $\varepsilon_{\text{a}}<\varepsilon_{\text{b}}$ (refer to the blue-colored straight lines in Figure 3). If the center of a crack Γ_m is the

origin, its accurate location can be retrieved for any nonzero ε_a. Same phenomenon can be examined for the case $\varepsilon_a = \varepsilon_b$ and $\mu_a \neq \mu_b$.

4. Numerical simulation results

In this section, we present some numerical simulation results with synthetic data to support Theorem 3.1. For the simulation, the homogeneous domain Ω was chosen as the unit circle centered at the origin, applied frequency of operation was selected as $f = 875$ MHz, and the incident direction $\boldsymbol{\theta}_n$ was chosen as in (2.3) with $N = 32$ based on recent studies [40, 54, 55]. With this configuration, the boundary measurement data in the absence and presence of small cracks and the adjoint problem (2.10) were obtained and solved by the finite element method (FEM), respectively. After the generation of the boundary measurement data, a 20dB Gaussian random noise was added to the unperturbed data.

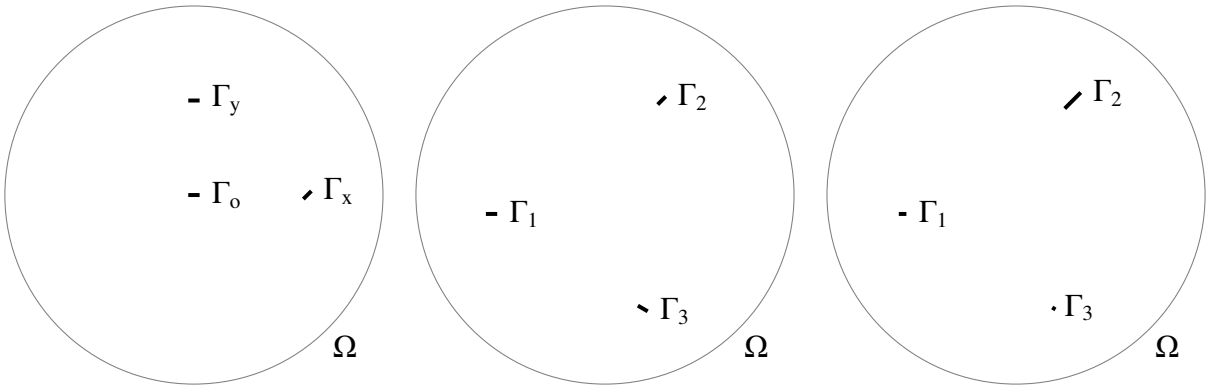

(a) Examples 4.1 and 4.2 (b) Example 4.3 (c) Example 4.4

Figure 4. Description of small cracks and homogeneous domain Ω.

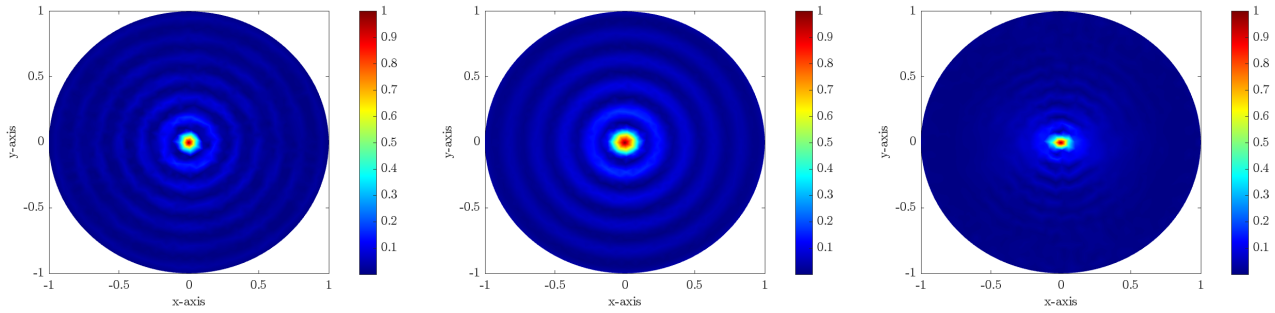

(a) $\varepsilon_a = \varepsilon_b$ (b) $\varepsilon_a = 0.6\varepsilon_b$ (c) $\varepsilon_a = 2.0\varepsilon_b$

Figure 5. (Example 4.1) Maps of $\mathfrak{F}(\mathbf{z}; k_a)$ with various ε_a at $f = 875$ MHz.

Example 4.1 (Single crack centered at the origin). We consider the identification of a single crack:

$$\Gamma_{\mathrm{o}} = \{(s, 0) : -0.03 \le s \le 0.03\}, \quad \mathbf{x}_{\mathrm{o}} = (0, 0).$$

Based on the imaging results in Figure 5, a peak of magnitude 1 appeared at the center. Hence, by regarding the maximum value of $\mathfrak{F}(\mathbf{z}; k_{\mathrm{a}})$, it is possible to recognize the exact location of Γ_{o} for any value of ε_{a}.

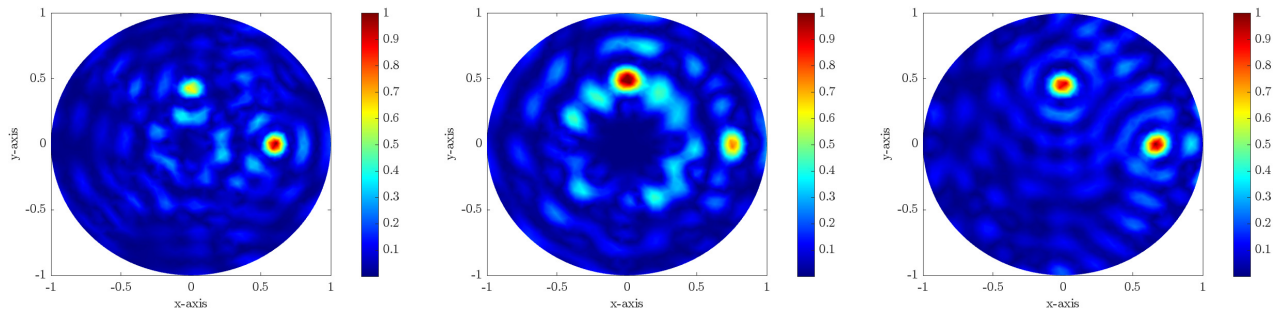

(a) $\varepsilon_{\mathrm{a}} = \varepsilon_{\mathrm{b}}$ (b) $\varepsilon_{\mathrm{a}} = 0.6\varepsilon_{\mathrm{b}}$ (c) $\varepsilon_{\mathrm{a}} = 0.8\varepsilon_{\mathrm{b}}$

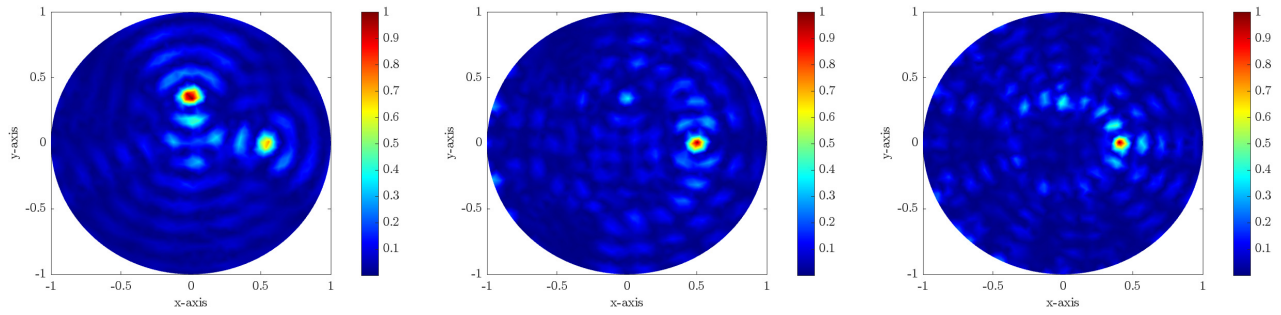

(d) $\varepsilon_{\mathrm{a}} = 1.2\varepsilon_{\mathrm{b}}$ (e) $\varepsilon_{\mathrm{a}} = 1.5\varepsilon_{\mathrm{b}}$ (f) $\varepsilon_{\mathrm{a}} = 2.0\varepsilon_{\mathrm{b}}$

Figure 6. (Example 4.2) Maps of $\mathfrak{F}(\mathbf{z}; k_{\mathrm{a}})$ with various ε_{a} at $f = 875$ MHz.

Example 4.2 (Two cracks whose centers are located on the axis). We consider the identification of two cracks with the same length:

$$\Gamma_{\mathrm{x}} = \{\mathcal{R}_{45^\circ}(s + 0.6, s) : -0.03 \le s \le 0.03\}, \qquad \mathbf{x}_{\mathrm{x}} = (0.6, 0),$$
$$\Gamma_{\mathrm{y}} = \{(s, 0.5) : -0.03 \le s \le 0.03\}, \qquad \mathbf{x}_{\mathrm{y}} = (0, 0.5),$$

where $\mathcal{R}_\theta$ denotes the rotation by θ. Based on the imaging results in Figure 6, we can examine that Γ_{x} is located somewhere along the x-axis; that is, while the exact y-coordinate of the center can be determined, the x-coordinate cannot. Similarly, Γ_{y} is located somewhere along the y-axis, but its true location and shape cannot be identified. It is interesting to note that if $\varepsilon_{\mathrm{a}} = \varepsilon_{\mathrm{b}}$, then the value of $\mathfrak{F}(\mathbf{z}; k_{\mathrm{a}})$ is greater when $\mathbf{z}$ lies on Γ_{x} than when it lies on Γ_{y}, but in the case where $\varepsilon_{\mathrm{a}} = 1.2\varepsilon_{\mathrm{b}}$, the situation is reversed. Finally, if $\varepsilon_{\mathrm{a}} \ge 1.5\varepsilon_{\mathrm{b}}$, it is very difficult to distinguish between Γ_{y} and several artifacts in the imaging results.

Example 4.3 (Three cracks with the same length). We consider the identification of three cracks with the same length:

$$\begin{aligned}
\Gamma_1 &= \{(s-0.6,-0.1) : -0.03 \le s \le 0.03\}, & \mathbf{x}_1 &= (-0.6,-0.1),\\
\Gamma_2 &= \{\mathcal{R}_{45^\circ}(s+0.3, s+0.5) : -0.03 \le s \le 0.03\}, & \mathbf{x}_2 &= (0.3, 0.5),\\
\Gamma_3 &= \{\mathcal{R}_{210^\circ}(s+0.2, s-0.6) : -0.03 \le s \le 0.03\}, & \mathbf{x}_3 &= (0.2,-0.6).
\end{aligned}$$

Figure 7 shows the maps of $\mathfrak{F}(\mathbf{z}; k_a)$ with various ε_a. Based on the imaging results, if the inaccurate value of k is applied, it is impossible to obtain accurate information about the x and y components of $\mathbf{x}_m$, $m = 1, 2, 3$, i.e., exact location of Γ_m cannot be retrieved. As we discussed in Property 3.2, the identified location of each $\mathbf{x}_m$ is close to the origin when $\varepsilon_a > \varepsilon_b$, and otherwise, the identified location of each $\mathbf{x}_m$ is located far from the origin when $\varepsilon_a < \varepsilon_b$. Moreover, contrary to the theoretical result, although all Γ_m have the same length, the value of $\mathfrak{F}(\mathbf{z}; k_a)$ at $\mathbf{z} \in \Gamma_3$ is smaller than at $\mathbf{z} \in \Gamma_1$ or Γ_2 when $\varepsilon_a = 0.6\varepsilon_b$ and $1.2\varepsilon_b$. Finally, similar to the results in Example 4.2, it is very difficult to distinguish between Γ_3 and several artifacts in the map of $\mathfrak{F}(\mathbf{z}; 2\varepsilon_b)$.

Example 4.4 (Three cracks with different lengths). For the final example, let us consider the identification of three cracks with different lengths:

$$\begin{aligned}
\Gamma_1 &= \{(s-0.6,-0.1) : -0.02 \le s \le 0.02\}, & \mathbf{x}_1 &= (-0.6,-0.1),\\
\Gamma_2 &= \{\mathcal{R}_{45^\circ}(s+0.3, s+0.5) : -0.06 \le s \le 0.06\}, & \mathbf{x}_2 &= (0.3, 0.5),\\
\Gamma_3 &= \{\mathcal{R}_{210^\circ}(s+0.2, s-0.6) : -0.01 \le s \le 0.01\}, & \mathbf{x}_3 &= (0.2,-0.6).
\end{aligned}$$

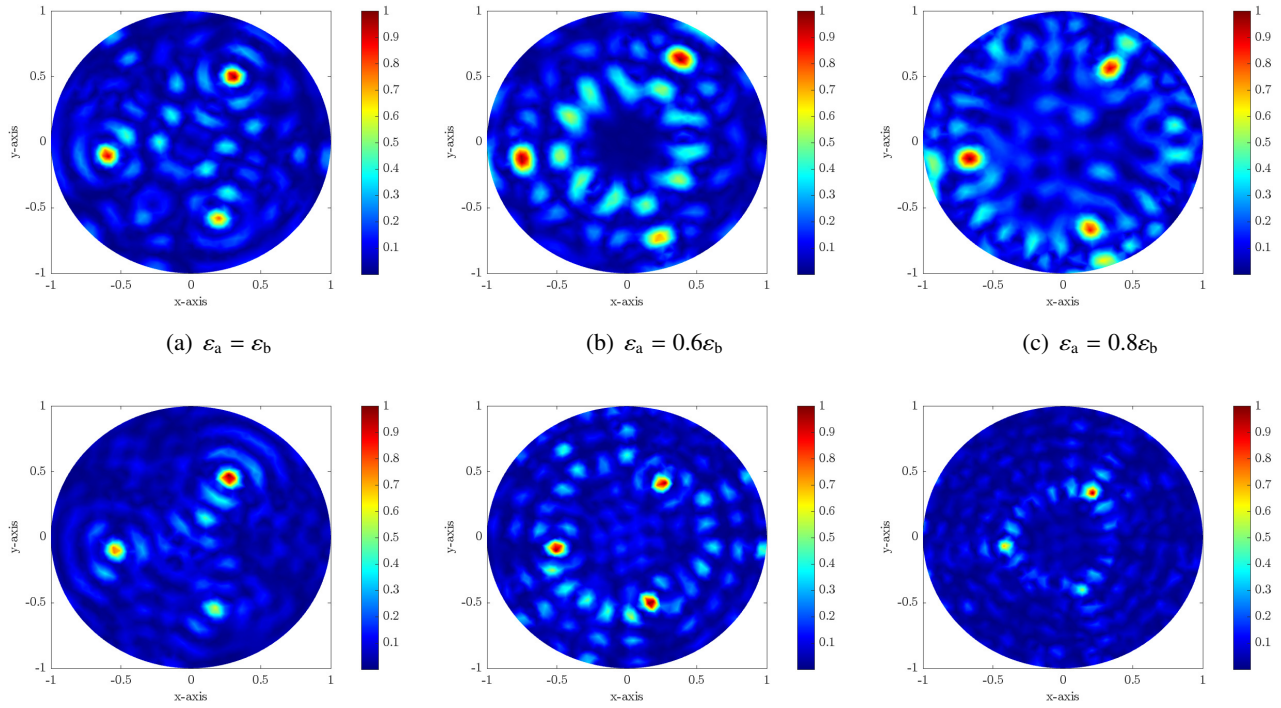

(a) $\varepsilon_a = \varepsilon_b$ (b) $\varepsilon_a = 0.6\varepsilon_b$ (c) $\varepsilon_a = 0.8\varepsilon_b$

(d) $\varepsilon_a = 1.2\varepsilon_b$ (e) $\varepsilon_a = 1.5\varepsilon_b$ (f) $\varepsilon_a = 2.0\varepsilon_b$

Figure 7. (Example 4.3) Maps of $\mathfrak{F}(\mathbf{z}; k_a)$ with various ε_a at $f = 875$ MHz.

Based on the imaging results in Figure 8, we can observe similar phenomena in Example 4.3. Independently of this, it is observed that Γ_3 is shorter than Γ_1 and Γ_2, resulting in the value of $\mathfrak{F}(\mathbf{z}; k_a)$ at $\mathbf{x}_3$ being significantly smaller than at $\mathbf{x}_1$ or $\mathbf{x}_2$.

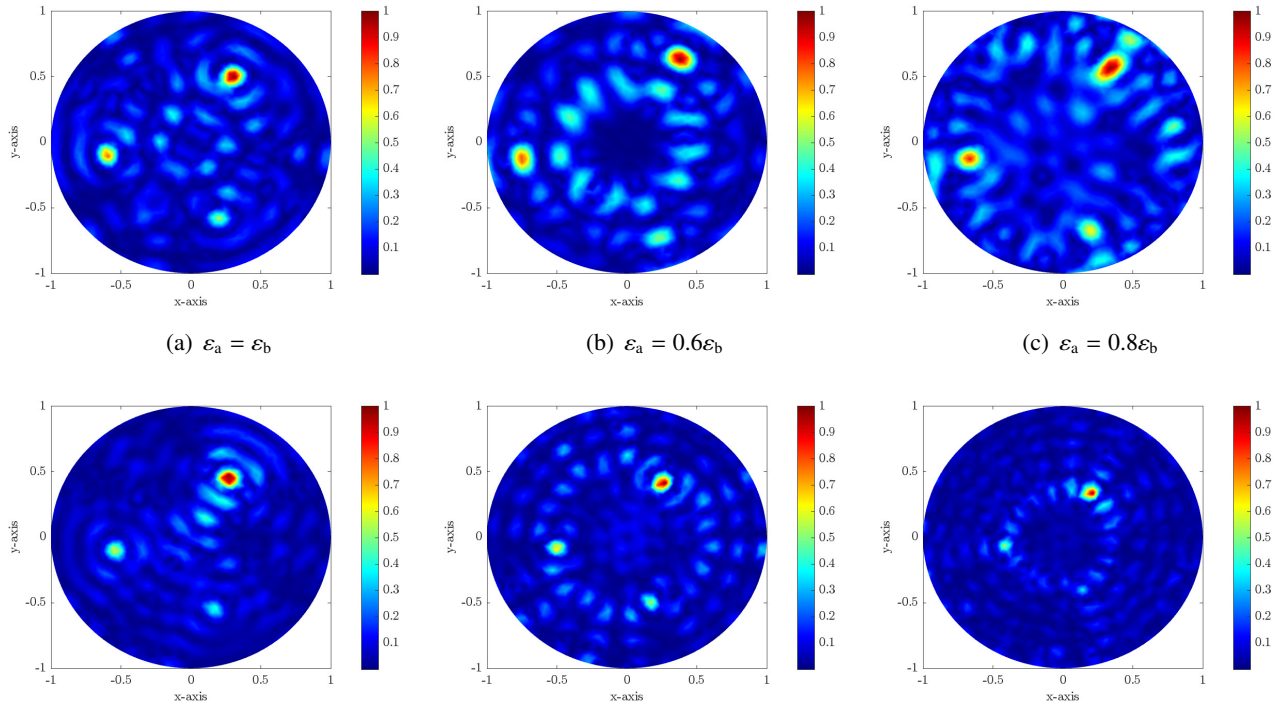

(a) $\varepsilon_a = \varepsilon_b$ (b) $\varepsilon_a = 0.6\varepsilon_b$ (c) $\varepsilon_a = 0.8\varepsilon_b$

(d) $\varepsilon_a = 1.2\varepsilon_b$ (e) $\varepsilon_a = 1.5\varepsilon_b$ (f) $\varepsilon_a = 2.0\varepsilon_b$

Figure 8. (Example 4.4) Maps of $\mathfrak{F}(\mathbf{z}; k_a)$ with various ε_a at $f = 875$ MHz.

5. Conclusions

We investigated the applicability of a topological derivative-based imaging technique for a fast identification of a set of small, linear perfectly conducting cracks completely embedded in a homogeneous domain with smooth boundary when accurate values of background permittivity and/or permeability are unknown. Based on the asymptotic expansion formula for the far-field pattern in the presence of cracks, we rigorously showed that the imaging function of a topological derivative can be expressed by the zero-order Bessel function and length of crack. Based on the discovered structure of the imaging function, we confirmed why the inaccurate location of cracks was reconstructed when there was an inaccurate value of background permittivity and/or permeability. To support the theoretical results, various numerical simulation results corrupted by random noise were exhibited.

In order to reconstruct cracks accurately, investigation of an imaging algorithm for retrieving the exact value of background permittivity and/or permeability would be a remarkable contribution to this study. In this paper, we considered an identification of two-dimensional cracks embedded in a homogeneous domain. Extension to the three-dimensional problem with an inhomogeneous domain and real-world applications will be important research subjects.

Use of Generative-AI tools declaration

The author declares he has not used Artificial Intelligence (AI) tools in the creation of this article.

Acknowledgments

The author would like to thank the anonymous reviewers for their valuable comments, which have helped improve the quality of the paper. This research was supported by the National Research Foundation of Korea (NRF) grant funded by the Korea government (MSIT) (RS-2025-16067902) and the research program of Kookmin University.

Conflict of interest

The author declare there is no conflict of interest.

References

1. O. S. Hassan, M. S. ur Rahman, A. A. Mustapha, S. Gaya, M. A. Abou-Khousa, W. J. Cantwell, Inspection of antennas embedded in smart composite structures using microwave NDT methods and X-ray computed tomography, *Measurement*, **226** (2024), 114086. https://doi.org/10.1016/j.measurement.2023.114086
2. M.-A. Ploix, V. Garnier, D. Breysse, J. Moysan, NDE data fusion to improve the evaluation of concrete structures, *NDT & E Int.*, **44** (2011), 442–448. https://doi.org/10.1016/j.ndteint.2011.04.006
3. X. Wu, X. Wei, H. Xu, W. He, C. Sun, L. Zhang, et al., Radar-absorbing materials damage detection through microwave images using one-stage object detectors, *NDT & E Int.*, **127** (2022), 102604. https://doi.org/10.1016/j.ndteint.2022.102604
4. D. Colton, P. Monk, The detection and monitoring of leukemia using electromagnetic waves: Numerical analysis, *Inverse Probl.*, **11** (1995), 329–341. https://doi.org/10.1088/0266-5611/11/2/003
5. M. Haynes, J. Stang, M. Moghaddam, Real-time microwave imaging of differential temperature for thermal therapy monitoring, *IEEE Trans. Biomed. Eng.*, **61** (2014), 1787–1797. https://doi.org/10.1109/TBME.2014.2307072
6. M. A. Islam, J. L. Volakis, Wearable microwave imaging sensor for deep tissue real-time monitoring using a new loss-compensated backpropagation technique, *IEEE Sens. J.*, **21** (2021), 3324–3334. https://doi.org/10.1109/JSEN.2020.3023482
7. H. Ammari, An Introduction to Mathematics of Emerging Biomedical Imaging, In: *Mathematics and Applications Series,* Springer, Berlin, 2008.
8. H. Ammari, Mathematical Modeling in Biomedical Imaging II: Optical, Ultrasound, and Opto-Acoustic Tomographies, In: *Lecture Notes in Mathematics,* Springer, Berlin, 2011. https://doi.org/10.1007/978-3-642-22990-9
9. R. Chandra, H. Zhou, I. Balasingham, R. M. Narayanan, On the opportunities and challenges in microwave medical sensing and imaging, *IEEE Trans. Biomed. Eng.*, **62** (2015), 1667–1682. https://doi.org/10.1109/TBME.2015.2432137

10. C. Bhat, M. A. Maisto, U. K. Khankhoje, R. Solimene, Subsurface radar imaging by optimizing sensor locations in spatio-spectral domains, *IEEE Trans. Geosci. Remote Sens.*, **61** (2023), 4505310. https://doi.org/10.1109/TGRS.2023.3305154

11. M. Cheney, A mathematical tutorial on synthetic aperture radar, *SIAM Rev.*, **43** (2001), 301–312. https://doi.org/10.1137/S0036144500368859

12. D. Tajik, R. Kazemivala, J. Nguyen, N. K. Nikolova, Accurate range migration for fast quantitative Fourier-based image reconstruction with monostatic radar, *IEEE Trans. Microw. Theory Tech.*, **70** (2022), 4273–4283. https://doi.org/10.1109/TMTT.2022.3187090

13. R. Kress, Inverse scattering from an open arc, *Math. Meth. Appl. Sci.*, **18** (1995), 267–293. https://doi.org/10.1002/mma.1670180403

14. T. Rubæk, P. M. Meaney, P. Meincke, K. D. Paulsen, Nonlinear microwave imaging for breast-cancer screening using Gauss–Newton's method and the CGLS inversion algorithm, *IEEE Trans. Antennas Propag.*, **55** (2007), 2320–2331. https://doi.org/10.1109/TAP.2007.901993

15. D. Ireland, K. Bialkowski, A. Abbosh, Microwave imaging for brain stroke detection using Born iterative method, *IET Microw. Antennas Propag.*, **7** (2013), 909–915. https://doi.org/10.1049/iet-map.2013.0054

16. O. Dorn, D. Lesselier, Level set methods for inverse scattering, *Inverse Probl.*, **22** (2006), R67–R131. https://doi.org/10.1088/0266-5611/22/4/R01

17. J. J. Mallorqui, N. Joachimowicz, A. Broquetas, J. C. Bolomey, Quantitative images of large biological bodies in microwave tomography by using numerical and real data, *Electron. Lett.*, **32** (1996), 2138–2140. https://doi.org/10.1049/el:19961409

18. H. Ammari, P. Garapon, F. Jouve, H. Kang, M. Lim, S. Yu, A new optimal control approach for the reconstruction of extended inclusions, *SIAM J. Control. Optim.*, **51** (2013), 1372–1394. https://doi.org/10.1137/100808952

19. A. A. Novotny, J. Sokolowski, Topological derivatives in shape optimization, In: *Interaction of Mechanics and Mathematics,* Springer Berlin, Heidelberg, 2013. https://doi.org/10.1007/978-3-642-35245-4

20. M. Bonnet, Fast identification of cracks using higher-order topological sensitivity for 2-D potential problems, *Eng. Anal. Bound. Elem.*, **35** (2011), 223–235. https://doi.org/10.1016/j.enganabound.2010.08.007

21. M. Bonnet, B. Guzina, N. Nemitz, Fast non-iterative methods for defect identification, *Rev. Eur. Mecan. Num.*, **17** (2008), 571–582. https://doi.org/10.13052/REMN.17.571-582

22. W.-K. Park, Multi-frequency topological derivative for approximate shape acquisition of curve-like thin electromagnetic inhomogeneities, *J. Math. Anal. Appl.*, **404** (2013), 501–518. https://doi.org/10.1016/j.jmaa.2013.03.040

23. F. L. Louër, M.-L. Rapún, Topological sensitivity for solving inverse multiple scattering problems in 3D electromagnetism. Part I: one step method, *SIAM J. Imag. Sci.*, **10** (2017), 1291–1321. https://doi.org/10.1137/17M1113850

24. S. Muñoz, M.-L. Rapún, Towards flaw detection in welding joints via multi-frequency topological derivative methods, *Comput. Math. Appl.*, **161** (2024), 121–136. https://doi.org/10.1016/j.camwa.2024.02.039
25. A. Carpio, M. Pena, M.-L. Rapún, Processing the 2D and 3D Fresnel experimental databases via topological derivative methods, *Inverse Probl.*, **37** (2021), 105012. https://doi.org/10.1088/1361-6420/ac21c8
26. N. Nemitz, M. Bonnet, Topological sensitivity and FMM-accelerated BEM applied to 3d acoustic inverse scattering, *Eng. Anal. Bound. Elem.*, **32** (2008), 957–970. https://doi.org/10.1016/j.enganabound.2007.02.006
27. M. Mobbet, F. Cakoni, Analysis of topological derivative as a tool for qualitative identification, *Inverse Probl.*, **35** (2019), 104007. https://doi.org/10.1088/1361-6420/ab0b67
28. M. Pena, M.-L. Rapún, Application of the topological derivative to post-processing infrared time-harmonic thermograms for defect detection, *J. Math. Industry*, **10** (2020), 4. https://doi.org/10.1186/s13362-020-0072-9
29. H. Ammari, J. Garnier, V. Jugnon, H. Kang, Stability and resolution analysis for a topological derivative based imaging functional, *SIAM J. Control. Optim.*, **50** (2012), 48–76. https://doi.org/10.1137/100812501
30. M. Burger, B. Hackl, W. Ring, Incorporating topological derivatives into level-set methods, *J. Comput. Phys.*, **194** (2004), 344–362. https://doi.org/10.1016/j.jcp.2003.09.033
31. A. Carpio, T. G. Dimiduk, F. L. Louër, M.-L. Rapún, When topological derivatives met regularized Gauss–Newton iterations in holographic 3D imaging, *J. Comput. Phys.*, **388** (2019), 224–251. https://doi.org/10.1016/j.jcp.2019.03.027
32. A. Carpio, M.-L. Rapún, Hybrid topological derivative and gradient-based methods for electrical impedance tomography, *Inverse Probl.*, **28** (2012), 095010. https://doi.org/10.1088/0266-5611/28/9/095010
33. L. He, C.-Y. Kao, S. Osher, Incorporating topological derivatives into shape derivatives based level-set methods, *J. Comput. Phys.*, **225** (2007), 891–909. https://doi.org/10.1016/j.jcp.2007.01.003
34. A. Blicher, K. Wodzinska, M. Fidorra, M. Winterhalter, T. Heimburg, The temperature dependence of lipid membrane permeability, its quantized nature, and the influence of anesthetics, *Biophys. J.*, **96** (2009), 4581–4591. https://doi.org/10.1016/j.bpj.2009.01.062
35. K. Chang, *Encyclopedia of RF and Microwave Engineering*, John Wiley & Sons, Inc., 2005.
36. J. A. Kong, *Electromagnetic Wave Theory*, EMW Publishing, 2008.
37. P. M. Meaney, S. A. Pendergrass, M. W. Fanning, D. Li, K. D. Paulsen, Importance of using a reduced contrast coupling medium in 2D microwave breast imaging, *J. Electromagn. Waves Appl.*, **17** (2003), 333–355. https://doi.org/10.1163/156939303322235851
38. D. M. Pozar, *Microwave Engineering*, 4th edition, John Wiley & Sons, Inc., 2011.
39. W.-K. Park, Topological derivative strategy for one-step iteration imaging of arbitrary shaped thin, curve-like electromagnetic inclusions, *J. Comput. Phys.*, **231** (2012), 1426–1439. https://doi.org/10.1016/j.jcp.2011.10.014

40. W.-K. Park, Investigation of a non-iterative technique based on topological derivatives for fast localization of small conductivity inclusions, *Comput. Math. Appl.*, **120** (2022), 45–59. https://doi.org/10.1016/j.camwa.2022.06.022
41. M. Abdelwahed, M. Hassine, M. Masmoudi, Control of a mechanical aeration process via topological sensitivity analysis, *J. Comput. Appl. Math.*, **228** (2009), 480–485. https://doi.org/10.1016/j.cam.2008.08.035
42. J. Céa, S. Garreau, P. Guillaume, M. Masmoudi, The shape and topological optimization connection, *Comput. Meth. Appl. Mech. Eng.*, **188** (2001), 703–726. https://doi.org/10.1016/S0045-7825(99)00357-6
43. P. Guillaume, K. S. Idris, The topological asymptotic expansion for the dirichlet problem, *SIAM J. Control. Optim.*, **41** (2002), 1042–1072. https://doi.org/10.1137/S0363012901384193
44. D. Auroux, M. Masmoudi, Image processing by topological asymptotic expansion, *J. Math. Imaging Vision*, **33** (2009), 122–134. https://doi.org/10.1007/s10851-008-0121-2
45. H. Ammari, H. Kang, H. Lee, W.-K. Park, Asymptotic imaging of perfectly conducting cracks, *SIAM J. Sci. Comput.*, **32** (2010), 894–922. https://doi.org/10.1137/090749013
46. H. Ammari, H. Kang, Reconstruction of Small Inhomogeneities from Boundary Measurements, In: *Lecture Notes in Mathematics,* Springer-Verlag, Berlin, 2004. https://doi.org/10.1007/b98245
47. H. Ammari, H. Kang, H. Lee, Layer Potential Techniques in Spectral Analysis, *Mathematical surveys and monographs*, American Mathematical Society, 2009. https://doi.org/10.1090/surv/153/10
48. H. Ammari, M. Vogelius, D. Volkov, Asymptotic formulas for perturbations in the electromagnetic fields due to the presence of imperfections of small diameter II. the full Maxwell equations, *J. Math. Pures Appl.*, **80** (2001), 769–814. https://doi.org/10.1016/S0021-7824(01)01217-X
49. E. Beretta, E. Francini, Asymptotic formulas for perturbations of the electromagnetic fields in the presence of thin imperfections, *Contemp. Math.*, **333** (2003), 49–63. https://doi.org/10.1090/conm/333/05953
50. E. Beretta, E. Francini, M. Vogelius, Asymptotic formulas for steady state voltage potentials in the presence of thin inhomogeneities. a rigorous error analysis, *J. Math. Pures Appl.*, **82** (2003), 1277–1301. https://doi.org/10.1016/S0021-7824(03)00081-3
51. D. R. Matteo, M. L. de Cristoforis, P. Musolino, *Singularly Perturbed Boundary Value Problems: A Functional Analytic Approach*, Springer Cham, 2021.
52. V. Maz'ya, A. Movchan, M. Nieves, Green's kernels and meso-scale approximations in perforated domains, In: *Lecture Notes in Mathematics,* Springer, Heidelberg, 2013. https://doi.org/10.1007/978-3-319-00357-3
53. W.-K. Park, Multi-frequency subspace migration for imaging of perfectly conducting, arc-like cracks in full- and limited-view inverse scattering problems, *J. Comput. Phys.*, **283** (2015), 52–80. https://doi.org/10.1016/j.jcp.2014.11.036
54. S. Kang, S. Chae, W.-K. Park, A study on the orthogonality sampling method corresponding to the observation directions configuration, *Res. Phys.*, **33** (2022), 105108. https://doi.org/10.1016/j.rinp.2021.105108

55. W.-K. Park, Topological derivative-based technique for imaging thin inhomogeneities with few incident directions, *Inverse Probl. Sci. Eng.*, **26** (2018), 1490–1508. https://doi.org/10.1080/17415977.2017.1411913

AIMS Press